Nanoscale
Horizons

ROYAL SOCIETY
OF CHEMISTRY

COMMUNICATION

View Article Online
View Journal | View Issue

Cite this: *Nanoscale Horiz.*, 2025, **10**, 2094

Received 7th April 2025,
Accepted 20th June 2025

DOI: 10.1039/d5nh00212e

rsc.li/nanoscale-horizons

One-step construction of NH_2-UiO-66 based heterojunction photocatalysts for adsorption–photocatalytic synergistic removal of antibiotics†

Yong Li,*[a] Xinyue Yang,[a] Deyun Yue,[a] Xiao Miao,[b] Mengyao Wang[a] and Haojie Song*[a]

Metal–organic frameworks (MOFs), as novel crystalline materials, exhibit notable photocatalytic activity and exceptional adsorption capabilities. However, their low charge separation efficiency still limits their photocatalytic performance. Herein, NH_2-UiO-66/BiOCl composites were synthesized through a one-step green grinding method, effectively integrating adsorption and photocatalytic degradation mechanisms. The NH_2-UiO-66/BiOCl-50% composite demonstrated outstanding degradation efficiency (96.84%) for ciprofloxacin (CIP) within 60 min, with a rate constant (0.0432 min^{-1}) that is 3.6 and 2.1 times those of NH_2-UiO-66 and BiOCl, respectively. The removal performance of NH_2-UiO-66/BiOCl for CIP and the underlying adsorption–photocatalytic degradation mechanisms were thoroughly investigated in various water environments. The remarkable degradation performance is attributed to the excellent adsorption capacity and the effective formation of a heterojunction between NH_2-UiO-66 and BiOCl, which enhances electron–hole separation and transfer efficiency. The stability of the photocatalyst is demonstrated by cyclic testing. Moreover, $^{\bullet}O_2^-$ was identified as the main active species and the photocatalytic mechanisms of the composite were elucidated. This work provides valuable insights into the synergistic integration of adsorption and photocatalytic degradation for the treatment of antibiotic-contaminated wastewater.

New concepts

This work demonstrates the novel concept of synergistically integrating adsorption and photocatalytic degradation mechanisms through heterojunction engineering of MOF-based composites. The NH_2-UiO-66/BiOCl composite leverages the dual functionality of MOFs and semiconductor materials. A one-step green grinding synthesis method enables intimate interfacial contact, creating a heterojunction that not only enhances adsorption of pollutants but also promotes spatially separated charge carriers, significantly boosting photocatalytic efficiency. Existing MOF-photocatalyst composites often struggle with inefficient charge transfer and unstable interfaces. This work overcomes these limitations by designing a hierarchical heterostructure where NH_2-UiO-66 acts as an electron donor and adsorption reservoir, while BiOCl serves as a hole-rich photocatalyst. The composite achieves 96.84% CIP degradation within 60 minutes, surpassing individual components by 3.6 times (NH_2-UiO-66) and 2.1 times (BiOCl), attributed to enhanced electron–hole separation and interfacial charge transfer. It also demonstrates adaptability to diverse antibiotics (tetracycline, sulfamethoxazole) and environmental conditions (inorganic ions, varying concentrations), offering practical versatility absent in most single-component photocatalysts.This work redefines heterojunction engineering by integrating MOFs with semiconductor charge dynamics, emphasizing structural synergy over individual material optimization. It advances the design of multifunctional nanomaterials for complex environmental remediation, bridging the gap between nanoscale interfacial engineering and macroscale pollutant treatment efficiency.

1. Introduction

The rapid development of industrialization and human society has led to an increasingly severe problem of environmental pollution. Among them, water contamination is particularly critical.[1] The major source of water pollution includes industrial effluents, domestic sewage, agricultural runoff, and medical waste. Previous studies have demonstrated that a large number of drugs are discharged into the water environment annually, such as hormone drugs, anti-inflammatory drugs and antibiotics.[2] As a result, scientists have explored various methods for removing antibiotic pollutants from water, including electrochemical methods, Fenton reactions, biological treatment, photocatalysis and adsorption. However, biological treatment, electrochemical methods and Fenton reactions are often hindered by issues such as high costs, long processing times, high energy consumption, and limited reaction conditions.[3–7]

---

[a] *School of Materials Science & Engineering, Key Laboratory of Underground Cultural Relics Conservation Materials and Technology, Ministry of Education, Shaanxi University of Science & Technology, Xi' an, 710021, P.R. China. E-mail: yongli@sust.edu.cn, songhaojie@sust.edu.cn*

[b] *Shandong Key Laboratory of Optical Communication Science and Technology, School of Physics Science and Information Technology, Liaocheng University, Liaocheng 252000, China*

† Electronic supplementary information (ESI) available. See DOI: **https://doi.org/10.1039/d5nh00212e**

Adsorption technology is simple and efficient in treating antibiotic sewage. However, it merely transfers the pollutants rather than completely degrading them.[8] By contrast, photocatalytic technology has emerged as one of the most promising approaches owing to its green, efficient, and environmentally friendly nature. Adsorption of pollutants plays a critical role in the photocatalytic process by pre-concentrating pollutants on the catalyst surface, thereby enhancing degradation efficiency.[9,10] Therefore, designing novel photocatalysts with high adsorption properties is an effective way to improve the photocatalytic activity.

Metal–organic frameworks (MOFs) are innovative crystalline materials composed of metal ions or clusters and organic ligands, and have the advantages of excellent adsorption performance, high surface areas and abundant active sites.[11] However, MOFs typically exhibit low photocatalytic efficiency compared to traditional photocatalysts due to their poor charge separation and high carrier recombination rates. The combination of MOFs and semiconductors with appropriate band gaps is beneficial for the carrier separation to improve the photocatalytic efficiency.[12,13] Zhang *et al.*[14] prepared Bi/BiO_2-X-$Bi_2O_2CO_3$/BiOCl@Bi-MOF using hydrothermal and photodeposition methods. The Z-scheme heterojunction significantly enhanced electron–hole separation and led to a photocatalytic degradation efficiency of 94.6% for CTC. Luo *et al.*[15] prepared a high-efficiency MIL-88B(Fe)/ZnTi-LDH composite with both adsorption and photocatalytic activities, demonstrating excellent photocatalytic performance due to efficient charge carrier separation. Li *et al.*[16] used a one-step process to prepare Ti–In bimetallic MOFs, combining the advantages of Ti-MOF and In-MOF (large specific surface area) to enhance both adsorption and photocatalytic degradation. Although the combination of MOFs and semiconductors could lead to excellent photocatalytic performance, complex preparation processes involved limit their practical applications. Therefore, it remains a significant challenge to design a green and simple method for preparing photocatalysts with high absorption properties and photocatalytic activity for large-scale applications.

BiOCl is a promising photocatalyst due to its high stability, reactivity and favorable photocatalytic activity. However, its narrow light absorption range, poor adsorption properties, and high carrier recombination rates significantly restrict its practical application in photocatalysis. Interestingly, the light absorption range can be enhanced by compositing materials with a wide light absorption range, and the construction of heterojunctions can promote the separation of carriers, thus improving the photocatalytic activity. Herein, NH_2-UiO-66/BiOCl composites were synthesized *via* a facile one-step green grinding method. NH_2-UiO-66 exhibits excellent adsorption performance and its integration with BiOCl results in the formation of a heterojunction that enhances electron–hole separation and transfer efficiency, leading to synergistic effects between adsorption and photocatalytic degradation. Ciprofloxacin (CIP) was chosen as a model molecule to evaluate the adsorption and photocatalytic performance of NH_2-UiO-66/BiOCl. This study also explores the factors influencing CIP adsorption and photocatalytic degradation, including the catalyst content, antibiotic concentration, and environmental factors such as inorganic salt ions. And, the adaptation of NH_2-UiO-66/BiOCl to different antibiotics, such as tetracycline and sulfamethoxazole, was also discussed. Subsequently, the adsorption mechanism of the composite towards CIP was analyzed, and the generation of active species was examined to deduce the photocatalytic mechanisms. This study provides new insights into the synergism of adsorption and photocatalytic degradation, and the degradation mechanism of CIP.

2. Results and discussion

2.1. Crystal structures, morphologies, and chemical compositions

A three-dimensional flower-like structure is formed by the self-assembly of smooth, impurity-free nanosheets of BiOCl, as shown in Fig. 1b. Fig. 1c and d reveal that NH_2-UiO-66 displays a regular octahedral crystal structure with particle size distribution centered around an average diameter of 14.32 ± 3.58 nm. As depicted in Fig. 1e and f, BiOCl acts as a platform and is completely coated with NH_2-UiO-66; due to the interaction between charges during the grinding process, the $-NH_2$ group of NH_2-UiO-66 is protonated to $-NH_3^+$ in acidic environments, which makes the whole NH_2-UiO-66 particle positively charged producing a strong electrostatic attraction with the Cl^- terminal (negative) of BiOCl. NH_2-UiO-66 was successfully coated on the surface of BiOCl due to the minimization of the thermodynamically driven interfacial energy and the promotion of homogeneous compounding of the material during the grinding process (Fig. 1a). The interaction between BiOCl and NH_2-UiO-66 leads to the successful formation of a compact heterojunction between the two substances, which promotes charge separation and enhances photocatalytic activity. HR-TEM images of UB-50% are shown in Fig. 1g, in which a lattice fringe with a lattice distance of 0.739 nm corresponds to the (001) facet of BiOCl.[17] Furthermore, EDS mapping of UB-50% shows that C, Zr, O, Bi, Cl elements were uniformly distributed (Fig. 1h), confirming the successful synthesis of the sample.

In Fig. 2a, the characteristic diffraction peaks at 7.4° and 8.5° correspond to the (111) and (200) planes, respectively, which agree with the calculated characteristic peaks, indicating the successful synthesis of NH_2-UiO-66.[18] The diffraction peaks of BiOCl at 32.63°, 40.91°, 46.77°, 54.28° and 58.59° correspond to the (110), (112), (200), (211), and (212) crystal planes (JCPDS-06-0249).[19] Meanwhile, the peaks of UB-*x* fit well with the NH_2-UiO-66 and BiOCl peaks, confirming the successful combination of both components. The FT-IR spectra of UB-*x* in Fig. 2b further confirm the successful synthesis of UB-*x* composites. The two strong vibrational peaks of NH_2-BDC located at 1578 cm^{-1} and 1385 cm^{-1} correspond to the carboxyl functional group (–COOH), respectively. The peaks at 1255 cm^{-1} and 665 cm^{-1} correspond to the C–N stretching vibrations and the O–H bond in NH_2-BDC, respectively.[20] For the pristine NH_2-UiO-66, the characteristic peak appearing at 765 cm^{-1} is ascribed to the vibration of the Zr–O bond and the ligands, demonstrating that NH_2-UiO-66 was successfully prepared. For BiOCl, the variation band located at 527 cm^{-1} corresponds to the Bi–O bond stretching vibration.[21] All characteristic vibration peaks of NH_2-UiO-66 and BiOCl demonstrate the successful preparation of UB-*x*.

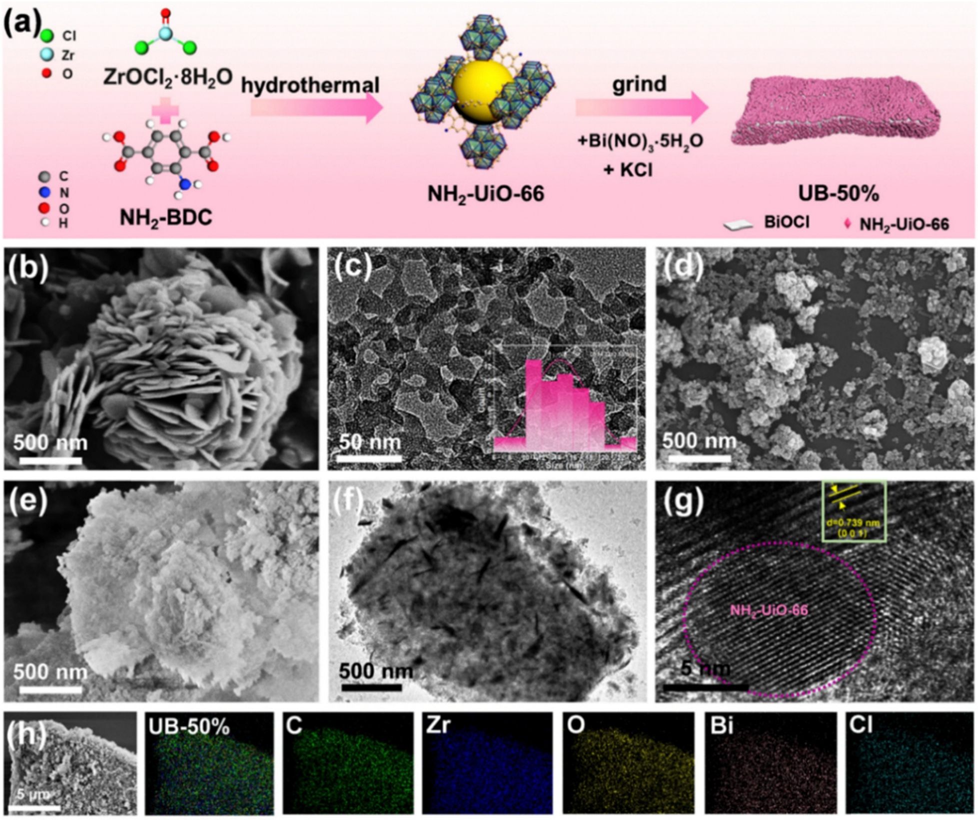

Fig. 1 (a) Schematic diagram of the preparation of NH_2-UiO-66/BiOCl. SEM images of BiOCl (b), NH_2-UiO-66 (d), and UB-50% (e). TEM images of the NH_2-UiO-66 (c) and UB-50% (f) and (g). EDS mapping images (h) of UB-50%.

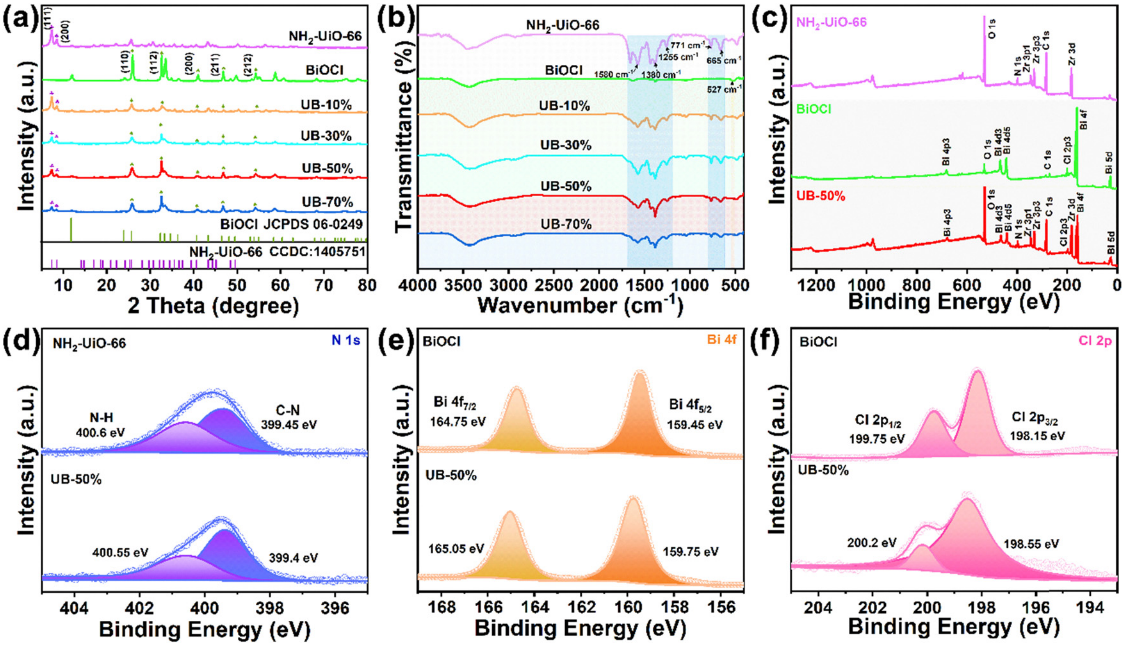

Fig. 2 The XRD patterns (a) and FT-IR spectra (b) of NH_2-UiO-66, BiOCl, and UB-*x*. The XPS spectra (c) and the high-resolution spectra of (d)–(f): N 1s, Bi 4f and Cl 2p of UB-50%.

The X-ray photoelectron spectra (XPS) of NH_2-UiO-66, BiOCl and UB-50% are presented in Fig. 2c. Bi, Cl, O, Zr, N and C elements were detected in UB-50% photocatalysts, with no additional impurities, consistent with the EDS results. In Fig. 2d, the N 1s binding energy peaks at 400.6 and 399.45 eV of NH_2-UiO-66 correspond to N–H and C–N bonds, respectively.[22] Compared to NH_2-UiO-66, the characteristic peaks of N–H and C–N for UB-50% were shifted to lower binding energies, which indicates an electron density increase of the N atom of NH_2-UiO-66 in UB-50%. In the Bi 4f spectrum of BiOCl (Fig. 2e), the two diffraction peaks located at 164.75 and 159.45 eV correspond to the Bi $4f_{7/2}$ and Bi $4f_{5/2}$ orbits of the trivalent oxidation state of Bi. As shown in Fig. 2f, the two characteristic peaks of Cl 2p at around 199.75 eV and 198.15 eV correspond to Cl $2p_{3/2}$ and Cl $2p_{1/2}$, respectively.[23] When NH_2-UiO-66 and BiOCl were combined by wet-grinding, the binding energy peaks of Bi 4f and Cl 2p were shifted to a higher binding energy. The shift of the binding energy peak demonstrates that BiOCl acts as the e^- donor and NH_2-UiO-66 acts as the e^- acceptor in UB-50%.

2.2. Adsorption performance

Fig. 3a–c shows the experimental results of N_2 adsorption–desorption. The isotherm of BiOCl belonged to type IV with an H3 shaped hysteresis loop, owing to the slit pores caused by plate slit construction and a crack and wedge structure, which coincided with the SEM results (Fig. 3a).[24] NH_2-UiO-66 exhibits a type IV isotherm with a H1 shaped hysteresis loop. The pore size of NH_2-UiO-66 is mainly concentrated within 5 nm (Fig. 3c), indicating the existence of mesopores.[25] In addition, NH_2-UiO-66 also exhibits a large specific surface area and high pore volume. NH_2-UiO-66 presents an excellent surface area (896.96 $m^2\ g^{-1}$). The comparison with other MOFs is shown in Table S1 (ESI†). BiOCl presents a low surface area (4.33 $m^2\ g^{-1}$), and the BET surface area of UB-50% is significantly improved compared to that of BiOCl, with a value of 552.11 $m^2\ g^{-1}$. In addition, the pore volume of UB-50% is as high as 0.81 $cm^3\ g^{-1}$. After the bonding of NH_2-UiO-66 and BiOCl by wet-grinding, UB-50% with a large specific surface area and high pore volume inherits the aperture characteristics of NH_2-UiO-66, and presents adsorption characteristics with a type-IV isotherm and a H1 shaped hysteresis loop (Fig. 3c). The high specific surface area and porosity of UB-50% are beneficial for the adsorption of CIP molecules.

Adsorption of reactants is one of the important processes in photocatalysis. Adsorption kinetics were analyzed using pseudo-first-order and pseudo-second-order models, as shown in Fig. 3d. The adsorption of CIP molecules rapidly increases within the first 10 min, reaching equilibrium after 30 min. The adsorption performances of UB-10%, UB-30%, UB-50% and UB-70% were obviously enhanced compared to that of BiOCl. The relevant parameters calculated using the pseudo-first order and pseudo-second order kinetic models are shown in Table 1. The values of correlation coefficients (R^2) of the first-order model of UB-*x* were smaller than those of the second-

Table 1 The best-fit model parameters of CIP adsorption kinetics onto samples

	Pseudo-first order			Pseudo-second order		
Sample	k_1 (min^{-1})	q_e ($mg\ g^{-1}$)	R^2	k_2 ($g\ mg^{-1}\ min^{-1}$)	q_e ($mg\ g^{-1}$)	R^2
NH_2-UiO-66	0.2791	30.67	0.9346	0.0236	30.64	0.9568
BiOCl	0.0567	1.43	1	0.0094	1.81	0.9793
UB-10%	0.2234	28.79	0.9633	0.0190	29.63	0.8801
UB-30%	0.1995	23.66	0.9446	0.0171	24.44	0.9705
UB-50%	0.1945	20.52	0.9436	0.0164	21.26	0.9804
UB-70%	0.1589	20.08	0.9538	0.0154	20.75	0.9706

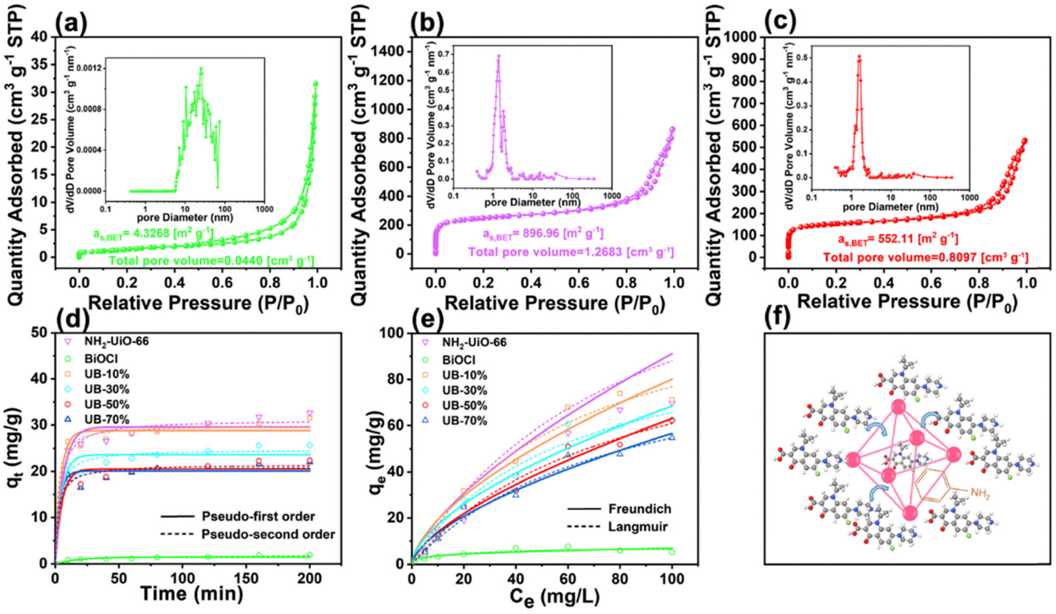

Fig. 3 Nitrogen adsorption–adsorption isotherm and pore size distribution plots of BiOCl (a), NH_2-UiO-66 (b) and UB-50% (c). Adsorption kinetics (d) and adsorption isotherms (e). Schematic diagram of the adsorption of NH_2-UiO-66 (f).

Table 2 The best-fit model parameters of CIP adsorption isotherms onto samples

	Langmuir model			Freundlich model		
Sample	q_m (mg g^{-1})	K_L (L mg^{-1})	R^2	K_F (mg g^{-1})/(mg L^{-n})	n	R^2
NH_2-UiO-66	91.20	0.0116	0.9724	4.0429	0.6765	0.9683
BiOCl	6.79	0.2600	0.7855	2.0811	0.1071	0.9047
UB-10%	79.90	0.0162	0.9679	4.628	0.6190	0.9541
UB-30%	68.55	0.0175	0.9640	4.2862	0.6016	0.9533
UB-50%	63.09	0.0125	0.9735	3.0673	0.6565	0.9777
UB-70%	56.66	0.0126	0.9921	3.2140	0.6233	0.9695

order model, which demonstrates that the chemisorption plays a critical role. The Langmuir and Freundlich isotherm models were used to fit the data of adsorption isotherm experiments. As shown in Fig. 3e, R^2 of the Langmuir model was higher than that of the Freundlich model (Table 2), which indicates that CIP formed a homogeneous adsorbed monolayer on UB-x.[26] According to the Langmuir model, the values of q_m of UB-x were all higher than that of BiOCl (6.79 mg g^{-1}). As previously reported, the unsaturated metal Zr sites of NH_2-UiO-66 easily interact with carbonyl, hydroxyl and amine groups on CIP molecules, promoting the adsorption of CIP (Fig. 3f).[27]

2.3. Optical and photoelectrochemical properties

The optical properties of the materials were studied using UV-visible diffuse reflectance spectroscopy (DRS). As shown in Fig. 4a, UV-vis DRS spectra demonstrated that NH_2-UiO-66 and BiOCl materials show characteristic peaks at around 463 nm and 367 nm. However, the absorption edge of UB-50% was redshifted to 468 nm, indicating enhanced visible light absorption due to the formation of the NH_2-UiO-66/BiOCl heterojunction. Generally, NH_2-UiO-66 and BiOCl are considered as direct bandgap semiconductors, and the corresponding band gaps can be estimated based on the Kubelka–Munk equation with results of 2.82 eV and 3.5 eV for NH_2-UiO-66 and BiOCl, respectively (Fig. 4b).[28,29] According to Mott–Schottky curves (Fig. 4c and d), NH_2-UiO-66 and BiOCl had positive slopes demonstrating that they were n-type semiconductors.[30,31] Therefore, the flat band potential was approximately considered to be the fermi level (E_f). Thus, the E_f values of NH_2-UiO-66 and BiOCl were −0.34 eV and −0.32 eV (*vs.* NHE) ($E_{fb\text{-}NHE}$ =

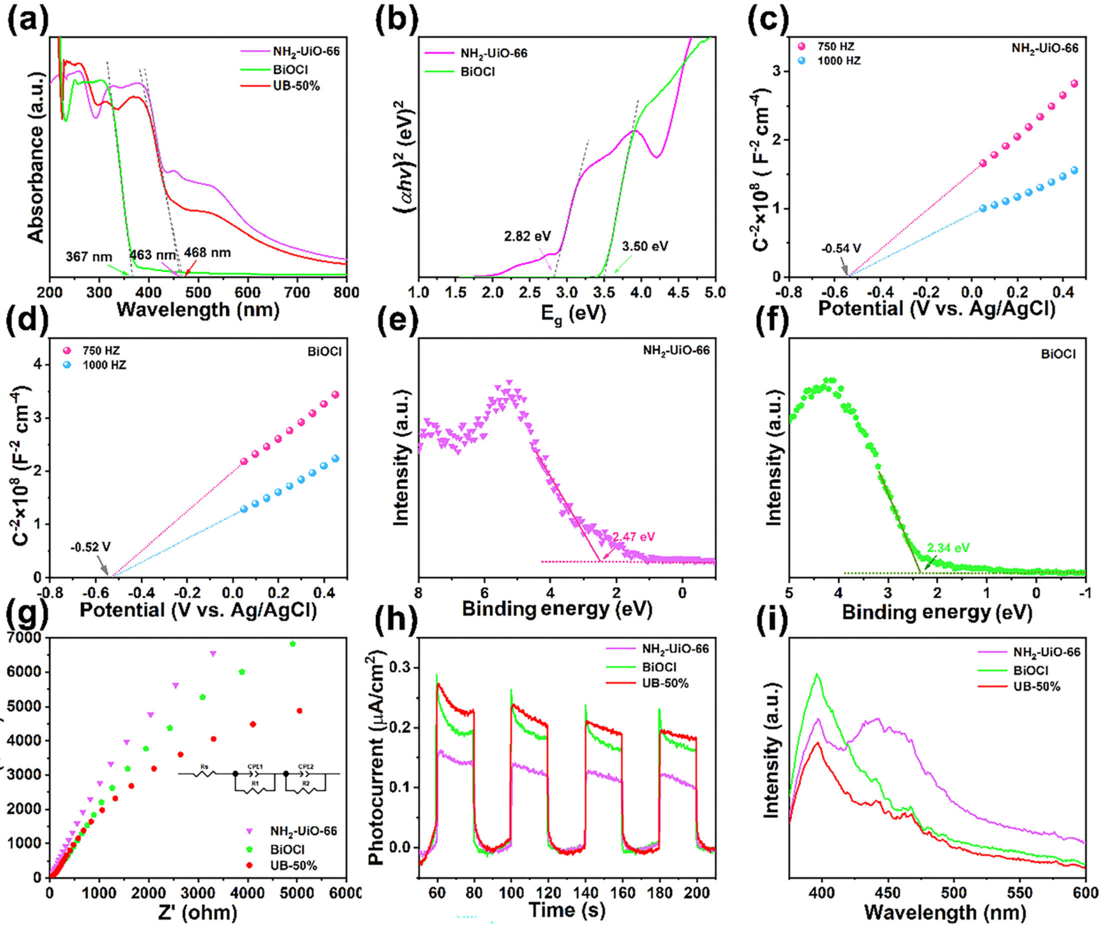

Fig. 4 UV-vis DRS spectra (a), the $(\alpha h\nu)^2$ *versus* E_g curves (b), Mott–Schottky plots (c) and (d), VB-XPS spectra (e) and (f), EIS Nyquist spectra (g), transient photocurrent densities (h) and photoluminescence spectra (i).

$E_{Ag/AgCl} + E^0_{Ag/AgCl}$), respectively. Furthermore, The VB-XPS of NH_2-UiO-66 and BiOCl are shown in Fig. 4e and f. They indicate that the energy gaps between the E_f and the VB were 2.47 eV and 2.34 eV for NH_2-UiO-66 and BiOCl, respectively.[32] Therefore, the E_{VB} values of NH_2-UiO-66 and BiOCl were calculated to be 2.13 eV and 2.02 eV, respectively. According to the equation ($E_{CB} = E_{VB} - E_g$), the E_{CB} values of NH_2-UiO-66 and BiOCl were −0.69 eV and −1.48 eV.[33]

Photoelectrochemical analysis of UB-50% was conducted using transient photocurrent responses, and the electrochemical impedance spectroscopy (EIS) results for equivalent circuits are presented in Table S2 (ESI†). The solution resistance (R_s) was considered as the resistance of the electrolyte/material interface, which was determined by the intercept on the Z' axis. The charge transfer resistance (R_{ct}) could be ascertained from the semicircle radius.[35] As shown in Fig. 4g, UB-50% showed the minimum semicircle radius, demonstrating the best photogenerated charge separation and transfer efficiency. Transient photocurrent responses were used to further study the charge transfer of UB-50%. As shown in Fig. 4h, UB-50% showed the best photocurrent response.[34] Furthermore, the photoluminescence (PL) spectroscopy results showed that UB-50% had the weakest PL intensity, suggesting that the heterojunction generated between NH_2-UiO-66 and BiOCl could reduce the recombination of photoinduced carriers and accelerate the transition and separation of e^- and h^+, which is consistent with the results of EIS and transient photocurrent responses (Fig. 4i).[36,37]

2.4. Photocatalytic performance

The photocatalytic performance of the as-prepared catalysts was evaluated to determine their light-driven CIP degradation efficiency, and optimal catalyst dosage and pollutant concentration were determined to find the optimal reaction parameters (Fig. 5). The removal efficiency of CIP decreased from 96.84% to 59.50% in 60 min with the concentration of CIP increasing from 10 mg L^{-1} to 60 mg L^{-1} (Fig. 5a) because of the insufficient active species generated from the limited amount of UB-50%. According to Fig. 5b, the degradation of CIP by UB-50% increased by about 45% as the catalyst dosage increased from 5 mg to 30 mg. In general, increasing the amount of the catalyst brings more reaction sites, which can promote photocatalytic activity. However, when the photocatalyst dosage was increased from 25 mg to 30 mg, the photodegradation efficiency was not significantly improved. According to previous studies, the increase of the photocatalyst concentration in the solution caused a shielding effect and reduced the light penetration, which was not beneficial to the photoreaction process.

Based on the optimized conditions of a CIP concentration of 20 mg L^{-1} and a catalyst dosage of 25 mg and the comparison of catalysts (NH_2-UiO-66/BiOCl/UB-*x*), the universality, reusability and the photocatalytic performance of UB-50% were

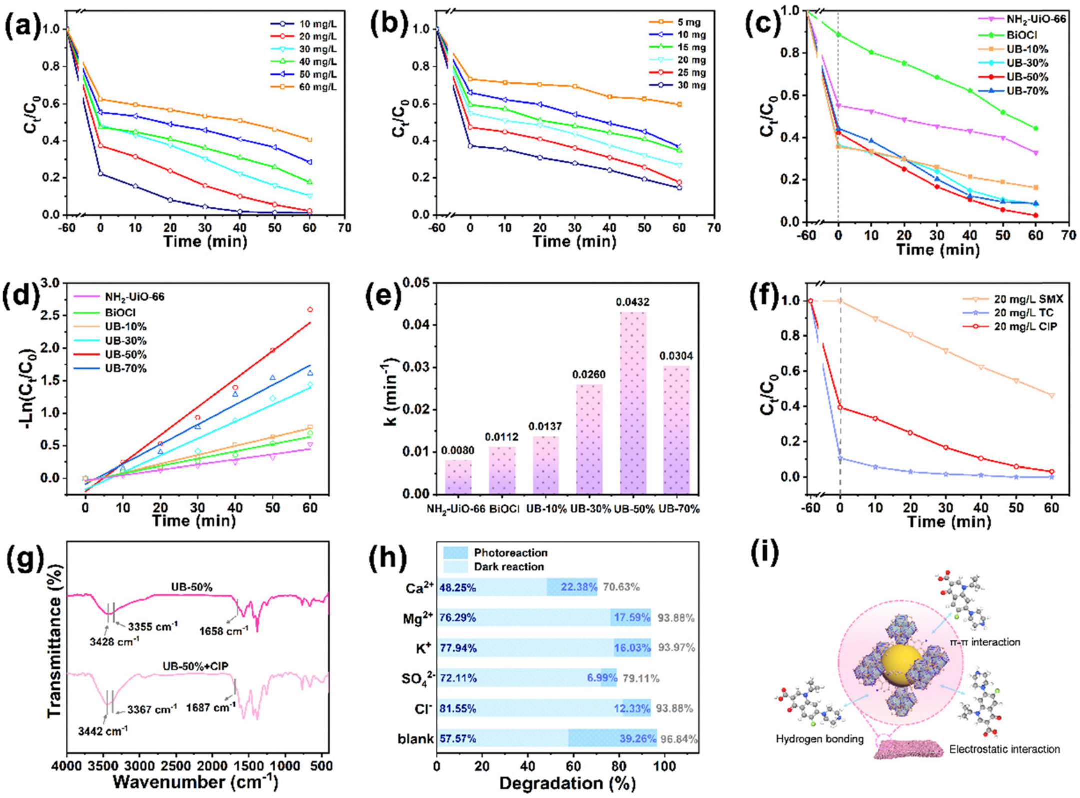

Fig. 5 Different concentrations (a), catalyst dosages of CIP (b), photocatalytic activity (c), first-order kinetic plots (d), and rate constants of NH_2-UiO-66, BiOCl and UB-*x* (e). Different antibiotics (f), FT-IR spectra (g), and ion co-existence for photocatalytic activity (h). Schematic diagram of the adsorption of UB-50% (i).

systematically studied. As seen in Fig. 5c and d, the degradation efficiency of CIP by BiOCl was only 74.30%. The degradation efficiencies of NH_2-UiO-66, UB-10%, UB-30%, UB-50%, and UB-70% were 81.50%, 83.81%, 91.45%, 96.84%, and 91.09%, respectively. In addition, the photodegradation removal rate of CIP by UB-50% was higher than those by NH_2-UiO-66 and BiOCl. The illumination time and removal efficiency of UB-*x* could linearly fit well with the first-order kinetics model ($-\ln(C_t/C_0) = k_t$).[38] The removal rate constants (k) are shown in Fig. 5e. The highest k value was 0.0432 min^{-1} for UB-50%, which was 3.6 times that of NH_2-UiO-66 (0.012 min^{-1}) and 2.1 times that of BiOCl (0.0209 min^{-1}). Furthermore, with the increase of the ratio of NH_2-UiO-66/BiOCl, the removal efficiency of CIP increased at first and then decreased, and UB-50% displayed the best degradation efficiency. Initially, the heterojunction of UB-*x* increases with the content of NH_2-UiO-66, promoting the separation of photogenerated charges and migration rates. However, excessive NH_2-UiO-66 covering the surface of BiOCl could affect the light absorption of BiOCl, causing the decline of degradation efficiency.

In order to investigate the universality of the UB-50% catalyst, CIP, tetracycline (TC) and sulfamethoxazole (SMX) were chosen as the target pollutants (Fig. 5f). The adsorption efficiency of UB-50% was evaluated in an antibiotic solution obtained by stirring for 60 min, and its adsorption reaches equilibrium in the dark. In addition, the adsorption capacity of UB-50% was less than 2% in SMX, about 60% in CIP and more than 90% in TC. In order to further explore the adsorption mechanism of UB-50%, in the aqueous solution of pH = 7 of UB-50%, the surface electric charge was determined by zeta potential. The zeta potential of UB-50% was negative (Fig. S1, ESI†). The two ionizable groups (carboxyl group and secondary amino group) of CIP could display different forms under acidic or alkaline conditions. CIP and TC existed in an amphoteric state in solution of pH = 7, and the positive charges are slightly more than the negative charges. Three mainly dissociating groups (tricarbonyl, phenolic dione and dimethylamino) of TC easily formed hydrogen bonds and electron donor–acceptor complexes, thus showing hydrophilicity and obvious adsorption.[39] Therefore, UB-50% exhibits excellent adsorption for TC. As SMX mainly shows negative charge under pH = 7 condition, it is difficult to adsorb SMX *via* electrostatic interactions by UB-50%.[40] Therefore, UB-50% can show 100% degradation efficiency for TC but only 53.53% for SMX under the above optimal reaction conditions after 60 min. The result indicates its excellent removal ability for positive antibiotics. Moreover, Fig. 5g shows the FT-IR spectra obtained before and after the adsorption of CIP on UB-50%. The absorption peaks at 3428 cm^{-1} and 3355 cm^{-1} were ascribed to the asymmetric and symmetric N–H stretching vibrations and N–H bending vibration of aromatic amines. The shift of the characteristic peaks of N–H and C=C indicates the existence of the hydrogen-bond interaction and π–π interaction between CIP and UB-50%.[41]

2.5. Factors affecting degradation activity

The actual water environment is composed of multiple components; therefore, the representative ions (Mg^{2+}, Ca^{2+}, K^+, Cl^-, and SO_4^{2-}) were added to the reaction system to explore the effect of ions on degradation of CIP by UB-50%. As shown in Fig. 5h, UB-50% presented satisfactory adsorption performance in CIP solution with Mg^{2+}, K^+, Cl^- and SO_4^{2-} except Ca^{2+}. The results showed that anions (Cl^- and SO_4^{2-}) had little influence on CIP adsorption. Meanwhile, cations coordinate with the functional groups of UB-50%, promoting the process of adsorption, which is mainly due to the cation chelation on CIP after addition of cations leading to rapid adsorption by UB-50%. In addition, the electrostatic repulsion effect of SO_4^{2-} and Cl^-, and negatively charged UB-50% weaken adsorption site competition. It can be concluded that Mg^{2+}, K^+, Cl^- and SO_4^{2-} had slightly enhanced the adsorption of CIP. However, Ca^{2+} likely occupied the adsorption sites of UB-50%, obstructing the adsorption of CIP.[42,43] It can be seen that cations (Mg^{2+}, K^+ and Ca^{2+}) had slight impacts on the CIP photoreaction, except for Cl^- and SO_4^{2-}. This was because SO_4^{2-} and Cl^- ions could act as radical scavengers, as shown in eqn (1) and (2).[44,45] As shown in Fig. 5i, chemisorption (hydrogen bonding and π–π interaction) and physisorption (electrostatic interaction) can be considered as the probable mechanisms of adsorption.

$$SO_4^{2-}/Cl^- + {}^{\bullet}OH \rightarrow SO_4^{\bullet-}/ClOH^{\bullet-} + OH^- \qquad (1)$$

$$SO_4^{2-}/ClOH^{\bullet-} + h^+ \rightarrow SO_4^{\bullet-}/Cl^{\bullet} \qquad (2)$$

2.6. The stability and photocatalytic mechanism

In practical applications, the stability and repeatability are of vital importance for photocatalysts. Thus, the stability of UB-50% was studied and the results are shown in Fig. 6a. The photocatalytic activity of UB-50% had no obvious loss after 5 cycles. Additionally, the fresh and used UB-50% tested by XRD revealed that the crystal structure and microstructure had no significant changes (Fig. 6b). The results indicate that UB-50% has excellent stability in degradation of antibiotics. The photodegradation mechanism and active species generated by UB-50% were investigated through radical trapping experiments on CIP. The quenching experiment employed *t*-butanol (*t*-BuOH), benzoquinone (BQ), and methanol (MeOH) as scavengers for the detection of ${}^{\bullet}OH$, ${}^{\bullet}O_2^-$, and h^+, respectively (Fig. 6c).[46] Compared to the removal efficiency of CIP without scavengers, the addition of *t*-BuOH and MeOH scavengers slightly restrained CIP degradation, indicating that ${}^{\bullet}OH$ and h^+ are not the key active species. Meanwhile, the degradation ratios of CIP obviously dropped to 18.39% with the addition of BQ. The results suggest that ${}^{\bullet}O_2^-$ plays the main role in the photocatalytic degradation of CIP, and ${}^{\bullet}OH$ radicals and h^+ play an auxiliary role in the degradation process.

NH_2-UiO-66 and BiOCl as single photocatalysts can still excite active species (${}^{\bullet}OH$, ${}^{\bullet}O_2^-$, and h^+) for CIP degradation. However, due to the high photogenerated electron–hole complexation efficiency of single-component photocatalysts (NH_2-UiO-66 and BiOCl), the active substances could not be generated efficiently. The energy band structure and the above-mentioned results of UB-50% indicate that NH_2-UiO-66 and

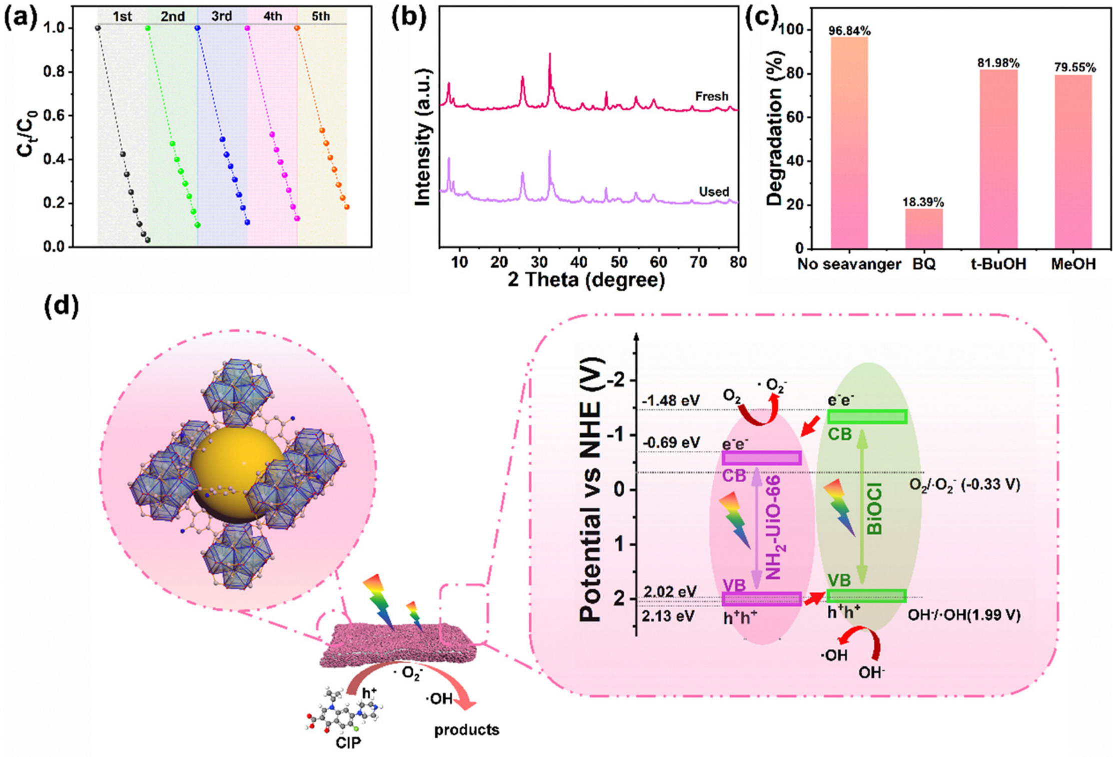

Fig. 6 Recycle test (a), XRD patterns (b), active species elimination experiments (c), and the possible mechanisms of UB-50% for CIP removal (d).

BiOCl easily form a type II heterojunction (Fig. 6d). After NH_2-UiO-66 and BiOCl come into contact, e^- flows from high E_f (BiOCl) to low E_f (NH_2-UiO-66) until the E_f is aligned. Due to electron accumulation, the NH_2-UiO-66 side energy band is negatively charged and bent downward. Due to hole accumulation, the BiOCl side energy band is bent upwards and positively charged, causing the formation of a built-in electric field.[47,48] The photogeneration of electron–hole pairs over BiOCl and NH_2-UiO-66, respectively, occurred upon the irradiation of UB-50% with full-light (eqn (3)). The photogenerated electrons from the CB position of BiOCl transferred to that of NH_2-UiO-66 (eqn (4)), and the holes moved from NH_2-UiO-66 to BiOCl (eqn (5)). Subsequently, the electrons on the surface of UB-50% reacted with O_2 to generate $^{\bullet}O_2^-$ (eqn (6)) and H_2O reacted with the holes to generate $^{\bullet}OH$ (eqn (7)), which oxidised CIP into CO_2, H_2O, and some small organic molecules (eqn (8)).

$$\text{UB-50\%} + h\nu \rightarrow \text{UB-50\%}\ (h^+ + e^-) \tag{3}$$

$$e^-\ (\text{BiOCl}) \rightarrow e^-\ (\text{NH}_2\text{-UiO-66}) \tag{4}$$

$$h^+\ (\text{NH}_2\text{-UiO-66}) \rightarrow h^+\ (\text{BiOCl}) \tag{5}$$

$$e^-\ (\text{NH}_2\text{-UiO-66}) + O_2 \rightarrow {}^{\bullet}O_2^- \tag{6}$$

$$h^+\ (\text{BiOCl}) + H_2O \rightarrow {}^{\bullet}OH + H^+ \tag{7}$$

$$\bullet OH + h^+ + \bullet O_2^-\ (\text{UB-50\%}) + \text{CIP} \rightarrow \text{degradation products} \tag{8}$$

3. Conclusions

In summary, UB-50% (NH_2-UiO-66/BiOCl) was synthesized using a facile one-step green grinding method at room temperature. CIP was selected as a model molecule to evaluate the adsorption and photocatalytic performance of NH_2-UiO-66/BiOCl. Among the tested composites, UB-50% showed excellent adsorption and photocatalytic properties. The composite exhibited excellent stability, as evidenced by repeatability experiments. The enhanced photocatalytic activities of UB-50% can be attributed to its remarkable adsorption capacity and the suitable construction of a heterojunction, which improves electron–hole separation and transfer efficiency. Additionally, $^{\bullet}O_2^-$ was identified as the main active species. Subsequently, the adsorption and photocatalytic mechanisms of the composite for CIP were analyzed. This work proposes a new approach for achieving adsorption and photocatalytic degradation synergistically.

Conflicts of interest

The authors declare no competing financial interest.

Data availability

The data supporting this article have been included as part of the ESI.†

Acknowledgements

The authors acknowledge funding from the National Natural Science Foundation of China (52303376), the Young Science and Technology Star Project of Shaanxi Province (2024), and The Youth Innovation Team of Shaanxi Universities (24JP027).

References

1 J. Wu, X. Y. Yang, X. H. Jia, J. Yang, X. Miao, D. Shao, H. J. Song and Y. Li, *Chem. Eng. J.*, 2023, **471**, 144684.

2 X. L. Liu, B. B. Huang, J. Li, B. J. Li and Z. Z. Lou, *Mater. Horiz.*, 2024, **11**, 5470–5498.

3 H. Xu, J. R. Li and X. X. Chu, *Nanoscale Horiz.*, 2023, **8**, 441–452.

4 T. Guo, X. Chen and L. F. Yin, *J. Mater. Chem. A*, 2024, **12**, 4397–4420.

5 G. Shahnazarova, N. A. H. A. Bast, J. C. Ramirez, J. Nogues, J. Esteve, J. Fraxedas, A. Serra, M. J. Esplandiu and B. Sepulved, *Mater. Horiz.*, 2024, **11**, 2206–2216.

6 X. Y. Li, S. H. Lin, R. R. Hu, P. Liang, Q. Y. Wu, B. B. Yang, S. Q. Lin, Q. L. Xu, J. N. Mei and J. Zou, *J. Opt. Photonics Res.*, 2025, DOI: **10.47852/bonviewJOPR52023222**.

7 Y. Li, X. Y. Yang, M. Y. Wang, D. Y. Yue, J. Wu and H. J. Song, *Sep. Purif. Technol.*, 2025, **361**, 131567.

8 Y. Li, X. Y. Yang, S. Yan, J. Yang, X. H. Jia and H. J. Song, *ACS Appl. Mater. Interfaces*, 2024, **16**, 1794–1804.

9 Y. C. Pan, L. J. Yang, G. Wang, H. Li, S. S. Wang, L. Zhang, W. Y. Wei and J. M. Lu, *ACS Appl. Mater. Interfaces*, 2024, **16**, 48836–48845.

10 O. Allam, M. Maghsoodi, S. S. Jang and S. D. Snow, *ACS Appl. Mater. Interfaces*, 2024, **16**, 36215–36223.

11 W. Wang, B. Ibarlucea, C. H. Huang, R. H. Dong, M. A. Aiti, S. R. Huang and G. Cuniberti, *Nanoscale Horiz.*, 2024, **9**, 1432–1474.

12 X. L. Huang, Y. Xing, H. Jiang, Y. Pu, S. Yang, Z. S. Kang and L. Cai, *J. Hazard. Mater.*, 2024, **472**, 134502.

13 Y. Chen, Y. Yang, S. Du, J. L. Ren, H. Jiang, L. B. Zhang and J. T. Zhu, *ACS Appl. Mater. Interfaces*, 2023, **15**, 35884–35894.

14 Y. Zhang, F. Y. Ma, M. H. Ling, H. Zheng, Y. T. Wu and L. Li, *Chem. Eng. J.*, 2023, **464**, 142762.

15 Y. D. Luo, G. Y. Shi, S. H. Yu, Z. T. Liu, J. W. Yin, M. S. Xue, Q. Sun, F. F. Shen, X. B. Li, Z. Z. Yin, C. Xie and B. Gao, *Chem. Eng. J.*, 2023, **473**, 145198.

16 M. M. Li, J. W. Yuan, G. Wang, L. J. Yang, J. X. Shao, H. Li and J. M. Lu, *Sep. Purif. Technol.*, 2022, **298**, 121658.

17 C. Dai, R. Z. Hu, C. M. Wang, Z. Liu, S. J. Zhang, L. D. Yu, Y. Chen and B. Zhang, *Nanoscale Horiz.*, 2020, **5**, 857–868.

18 S. Z. Zheng, H. Du, L. X. Yang, M. Tan, N. Y. Li, Y. J. Fu, D. Hao and Q. Wang, *J. Hazard. Mater.*, 2023, **447**, 130849.

19 Z. Q. Long, H. L. Wang, K. W. Huang, G. M. Zhang and H. J. Xie, *J. Hazard. Mater.*, 2022, **424**, 127554.

20 S. Y. Wang, Z. W. Ai, X. W. Niu, W. J. Yang, R. Kang, Z. G. Lin, A. Waseem, L. Jiao and H. L. Jiang, *Adv. Mater.*, 2023, **35**, 2302512.

21 Y. R. Chen, D. Y. Zhu, S. K. Xue, H. Y. Wang, Q. J. Lu, G. H. Ruan, C. X. Zhao and F. Y. Du, *Appl. Surf. Sci.*, 2024, **653**, 159337.

22 I. Akpinar, X. L. Wang, K. Fahy, F. R. Sha, S. L. Yang, T. W. Kwon, P. J. Das, T. Islamoglu, O. K. Farha and J. F. Stoddart, *J. Am. Chem. Soc.*, 2024, **146**, 5108–5117.

23 Z. H. Zhao, H. Wang, J. J. Li, X. Y. Qiao, Z. P. Liu, Z. P. Ren, M. L. Yuan and J. Zhang, *J. Am. Chem. Soc.*, 2024, **146**, 29441–29449.

24 B. H. Wang, J. F. Chen, J. B. Zhong, J. Z. Li and Y. B. Zhu, *Appl. Surf. Sci.*, 2024, **644**, 158750.

25 W. J. Qu, Z. L. Wang, M. Y. Qin, X. J. Yang, F. S. Zhang, Z. Wang, D. D. Ji and D. H. Yu, *Sep. Purif. Technol.*, 2023, **325**, 124673.

26 L. H. Meng, C. Zhao, T. Y. Wang, H. Y. Chu and C. C. Wang, *Sep. Purif. Technol.*, 2023, **313**, 123511.

27 Y. L. Dong, H. R. Liu, S. M. Wang, G. W. Guan and Q. Y. Yang, *ACS Catal.*, 2023, **13**, 2547–2554.

28 M. Pander, R. Gil-San-Millan, P. Delgado, C. Perona-Bermejo, U. Kostrzewa, K. Kaczkowski, D. J. Kubicki, J. A. R. Navarro and W. Bury, *Mater. Horiz.*, 2023, **10**, 1301–1308.

29 S. A. Ali, S. Sarkar and A. K. Patra, *ACS Appl. Mater. Interfaces*, 2024, **16**, 38061–38072.

30 A. Kuila, S. Pichiah, D. Bahnemann and C. Y. Wang, *Appl. Catal., B*, 2021, **293**, 120224.

31 Q. Wang, S. Z. Zheng, W. G. Ma, J. Y. Qian, L. Y. Huang, H. Deng, Q. Zhou, S. R. Zheng, S. J. Li, H. Du, Q. Li, D. Hao and G. X. Yang, *Appl. Catal., B*, 2024, **344**, 123669.

32 F. Zhao, D. Gao, X. M. Zhu, Y. M. Dong, X. Liu and H. X. Li, *Appl. Surf. Sci.*, 2022, **587**, 152780.

33 H. S. Zheng, B. Y. Zi, T. Zhou, G. Y. Qiu, Z. G. Luo, Q. J. Lu, A. R. P. Santiago, Y. M. Zhang, J. H. Zhao, J. Zhang, T. W. He and Q. J. Liu, *Nanoscale Horiz.*, 2024, **9**, 1532–1542.

34 F. H. Xu, Q. Q. Zhang, R. S. An, L. Li and L. M. Zhou, *J. Alloys Compd.*, 2022, **899**, 163324.

35 Y. Jiang, S. C. Liu, L. P. Zhang, G. W. Guan, Y. T. Li, S. Ni, R. Y. Jiang, S. T. Zheng, H. R. Liu, H. L. Lan and Q. Y. Yang, *Chem. Eng. J.*, 2024, **494**, 153100.

36 S. M. Obaidulla, A. Supina, S. Kamal, Y. Khan and M. Kralj, *Nanoscale Horiz.*, 2024, **9**, 44–92.

37 R. Li, Y. Li, X. H. Jia, J. Yang, X. Miao, D. Shao, J. Wu and H. J. Song, *Desalination*, 2024, **574**, 117295.

38 W. Y. Zhen, Y. Liu, X. D. Jia, L. Wu, C. Wang and X. Jiang, *Nanoscale Horiz.*, 2019, **4**, 720–726.

39 Q. Q. Ni, X. Ke, W. J. Qian, Z. Yan, J. D. Luan and W. G. Liu, *Appl. Catal., B*, 2024, **340**, 123226.

40 B. Zhang, S. Q. Xia, Z. Y. Wang, W. Q. Li, B. D. Li, H. C. Zhang, Y. Xin, J. Wu, K. J. Ma and X. He, *Appl. Catal., B*, 2024, **349**, 123861.

41 X. Z. Jiang, M. Wang, Z. C. Lou, H. Han, N. N. Yan, Q. B. Guan and L. Xu, *ACS Nano*, 2024, **18**(3), 2290–2301.

42 J. H. Gu, Z. Liu, A. Y. Jia, Y. Q. Wang, N. N. Li, Z. S. Liu, Y. X. Li and H. X. Zhang, *Sep. Purif. Technol.*, 2023, **312**, 123408.

43 J. H. Sha, L. L. Li, Z. X. An, M. X. He, H. Y. Yu, Y. Wang, B. Y. Gao and S. P. Xu, *Chem. Eng. J.*, 2022, **428**, 131065.

44 M. Abinaya, K. Govindan, M. Kalpana, K. Saravanakumar, S. L. Prabavathi, V. Muthuraj and A. Jang, *J. Hazard. Mater.*, 2020, **397**, 122885.

45 L. L. Liang, S. W. Gao, J. C. Zhu, L. J. Wang, Y. N. Xiong, X. F. Xia and L. W. Yang, *Chem. Eng. J.*, 2020, **391**, 123599.

46 Y. Y. Gu, J. X. Wang, Q. Q. Tang, H. T. Wei, J. Ning, X. F. Lan, X. F. Wang, X. H. Li, Y. G. Jia, S. B. Wang and L. Hao, *ACS Catal.*, 2024, **14**, 11262–11272.

47 T. Guo, G. J. Hu, C. W. Wang, J. X. Liu, G. M. Ren and Q. J. Guo, *J. Alloys Compd.*, 2025, **1022**, 179965.

48 M. Wen, Q. Guo, X. L. Liu, X. Li, H. P. Li, H. J. Zhan and W. Y. Liu, *Polyhedron*, 2025, **271**, 117420.